

Article

# Titanian Clinohumite-Bearing Peridotite from the Ulamertoq Ultramafic Body in the 3.0 Ga Akia Terrane of Southern West Greenland

Ikuya Nishio <sup>1</sup>, Tomoaki Morishita <sup>2,3,\*</sup> , Kristofer Szilas <sup>4</sup> , Graham Pearson <sup>5</sup>, Ken-Ichiro Tani <sup>6</sup>, Akihiro Tamura <sup>2</sup>, Yumiko Harigane <sup>7</sup> and Juan Miguel Guotana <sup>1</sup>

<sup>1</sup> Graduate School of Natural Science and Technology, Kanazawa University, Kanazawa, Ishikawa 920-1192, Japan; ikuyanishio240@gmail.com (I.N.); jmguotana@gmail.com (J.M.G.)

<sup>2</sup> Faculty of Geosciences and Civil Engineering, Institute of Science and Engineering, Kanazawa University, Kanazawa, Ishikawa 920-1192, Japan; aking826@gmail.com

<sup>3</sup> Lamont-Doherty Earth Observatory, Columbia University, New York, NY 10027, USA

<sup>4</sup> Department of Geosciences and Natural Resource Management, University of Copenhagen, 10, 1165 Copenhagen, Denmark; krsz@ign.ku.dk

<sup>5</sup> Department of Earth and Atmospheric Science, University of Alberta, Edmonton, AB T6G 2B4, Canada; gdpearso@ualberta.ca

<sup>6</sup> National Museum of Nature and Science, Tokyo 110-8718, Japan; kentani@kahaku.go.jp

<sup>7</sup> Institute of Geology and Geoinformation Geological Survey of Japan/AIST, Tsukuba, Ibaraki 305-8560, Japan; y-harigane@aist.go.jp

\* Correspondence: moripta@staff.kanazawa-u.ac.jp; Tel.: +81-(0)76-264-6513

Received: 27 December 2018; Accepted: 28 March 2019; Published: 1 April 2019



**Abstract:** A titanian clinohumite-bearing dunite was recently found in the Ulamertoq ultramafic body within the 3.0 Ga Akia Terrane of southern West Greenland. Titanian clinohumite occurs as disseminated and discrete grains. Titanian clinohumite contains relatively high amounts of fluorine, reaching up to 2.4 wt.%. The high-Fo content of olivine (Fo<sub>93</sub>) coupled with low Cr/(Cr + Al) ratio of orthopyroxene implies that the dunite host is not of residual origin after melt extraction by partial melting of the primitive mantle. Olivine grains are classified into two types based on abundances of opaque mineral inclusions: (1) dusty inclusion-rich and (2) clear inclusion-free olivines. Opaque inclusions in coarse-grained olivines are mainly magnetite. Small amounts of ilmenite are also present around titanian clinohumite grains. The observed mineral association indicates partial replacement of titanian clinohumite to ilmenite (+magnetite) and olivine following the reaction: titanian clinohumite = ilmenite + olivine + hydrous fluid. The coexistence of F-bearing titanian clinohumite, olivine, and chromian chlorite indicates equilibration at around 800–900 °C under garnet-free conditions (<2 GPa). Petrological and mineralogical characteristics of the studied titanian clinohumite-bearing dunite are comparable to deserpentinized peridotites derived from former serpentinites. This study demonstrates the importance of considering the effects of hydration/dehydration processes for the origin of ultramafic bodies found in polymetamorphic Archaean terranes.

**Keywords:** titanian clinohumite-bearing ultramafic rock; Archaean terrane; West Greenland; serpentinite; dehydration

## 1. Introduction

Archaean rocks are widely exposed in southern West Greenland. Several tectonomagmatic terranes comprise southern West Greenland, which can be sub-divided based on age and metamorphic evolution: from north to south the Akia, Akulleq, and Tasiusarsuaq terranes [1,2] (Figure 1a). Exposures

of ultramafic rocks are minor, but are important components of the Archaean terranes in southern West Greenland [3–10]. These ultramafic rocks could provide direct information on the evolution of the Earth's mantle. The origins of these ultramafic rocks and their tectonic settings are, however, still enigmatic [4,6,8–14]. Two conflicting origins are proposed for the ultramafic rocks in the Archaean terranes in southern West Greenland: (1) residue after partial melting, and (2) ultramafic cumulate formed by mafic mineral accumulation or crystallization from komatiitic melts [11,15]. The tectonic setting for these ultramafic rocks is also unclear. Whole rock and mineral compositions are similar to abyssal peridotites [6], whereas other chemical indicators suggest a potential subarc origin [12,14]. The B-type fabric of olivine, which is generally interpreted as hydrous deformation, was reported and also further supports a subarc origin [16] for these ultramafic rocks. It should be noted, however, that some ultramafic rocks in the 3.8–3.7 Ga Isua Supracrustal Belt (Akulleq terrane, Figure 1) are highly serpentinized, carbonatized and metasomatized [4,17,18]. In comparison to the ultramafic bodies in the Isua Supracrustal Belt, the ultramafic bodies of the Akia terrane have not been studied in detail.

The Ulamertoq ultramafic body (1 km × 1.5 km in size) is the largest ultramafic body in the Akia terrane [5,9,11]. In this ultramafic body, a titanian clinohumite-bearing peridotite was recently identified and is the focus of the present study. Titanian clinohumite ( $M_8Si_4O_{16}M_{1-x}Ti_x(OH)_{2-2x}O_{2x}$ , where M is Mg,  $Fe^{2+}$ , Mn and Ni and  $x > 0.5$ ) [19–21] is an important hydrous mineral in ultramafic rocks [22,23]. Titanian clinohumite-bearing ultramafic rocks are reported to be exposed as part of the ultramafic bodies in the Isua Supracrustal Belt [12,24]. Titanian clinohumite is also reported from mantle xenoliths [22,23,25,26] and metamorphosed ultramafic rocks [27–36]. In this study, we document the petrology and mineral chemistry of this new titanian clinohumite-bearing ultramafic rock from the Akia terrane and discuss the pressure-temperature conditions for its genesis, as well as its implication for the tectonic evolution in the studied area.

## 2. Sampling Locality and Methods

### 2.1. Geological Background

The Ulamertoq ultramafic body occurs within the amphibolite-granulite facies orthogneiss of the 3.0 Ga Akia terrane [37–39]. Small ultramafic lenses, a few meters to a few tens of meters in size, are also commonly observed in the orthogneiss around the Ulamertoq body [5,9,11]. Norite is observed in the northeastern part of this ultramafic body. Granitic rocks that locally cut the ultramafic body are commonly present (Figure 1c).

Ultramafic rocks in Ulamertoq are heterogeneous in mineral mode (Figure 2). Phlogopite and amphiboles are frequently observed in the Ulamertoq peridotite and locally dominate at the boundary with the surrounding orthogneiss (Figure 2a). Harzburgite to amphibole-bearing orthopyroxenite are also present (Figure 2b,c). Chromitite layers are rare, and their host rocks are variable in mineral modes [40]. Dunitic rocks are dominant in the Ulamertoq body, although modal abundances of orthopyroxene and amphibole are variable from locality to locality. We examined 9 representative ultramafic samples and only one dunite sample contains titanian clinohumite. Dunitic rocks including the studied titanian clinohumite-bearing peridotite (Figure 2d), occur far from the surrounding gneiss (Figure 1c). It is essentially impossible to identify titanian clinohumite-bearing peridotite in the field. Therefore, it is not currently clear what the spatial extent of titanian clinohumite-bearing rocks are within the Ulamertoq ultramafic body.

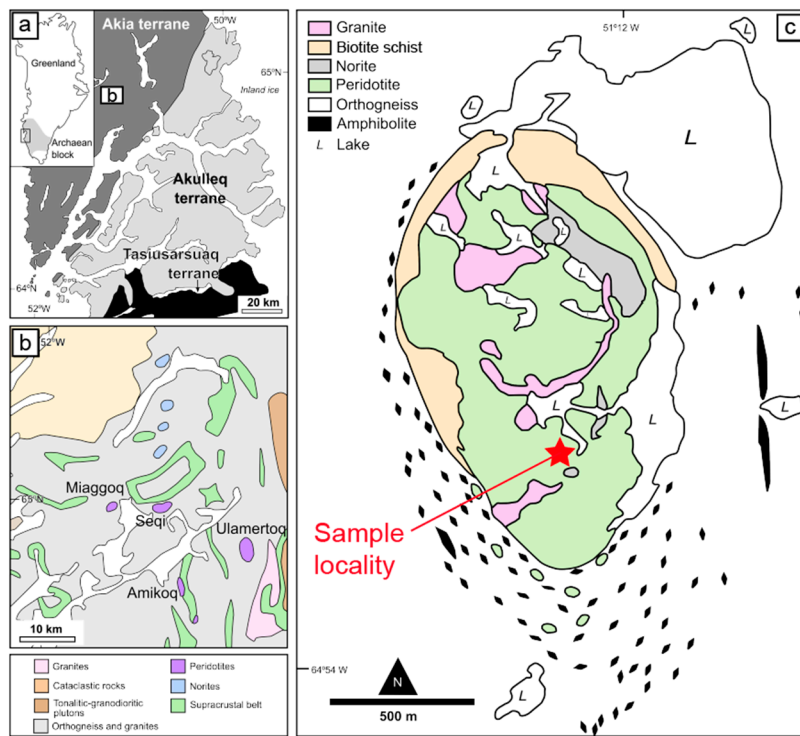


**Figure 1.** (a) Simplified geological map of the Nuuk region of southern West Greenland after [1]; (b) Map showing various peridotite bodies in the central part of the Akia Terrane after [15]; (c) Simplified lithological map of the Ulamertog peridotite body after [5] showing the sample locality of the studied titanite-bearing peridotite.

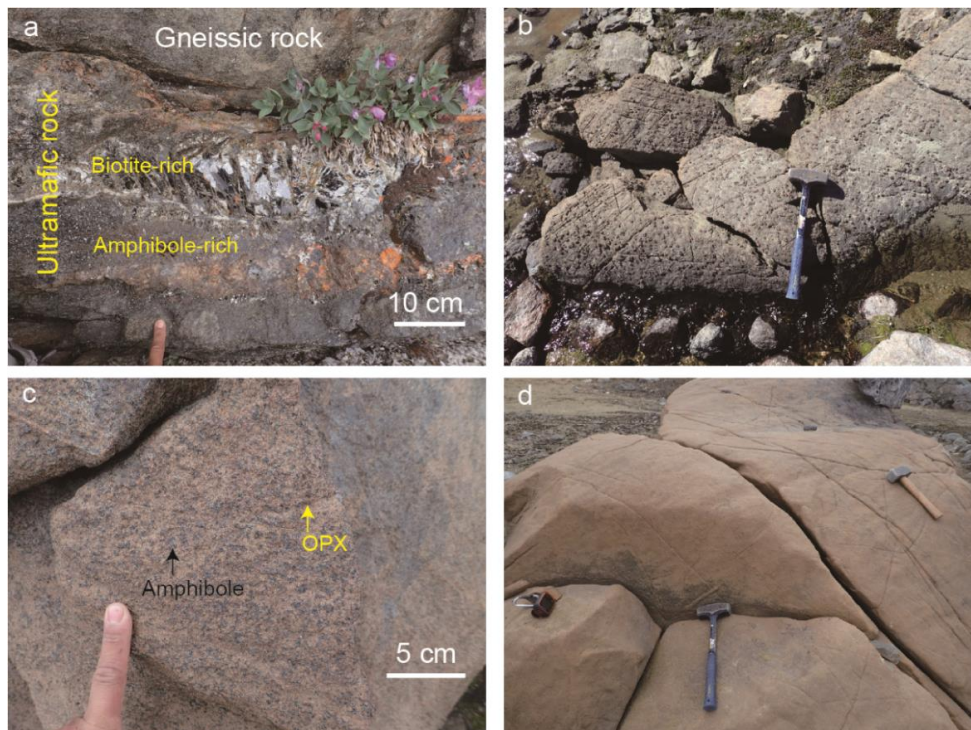


**Figure 2.** (a) Biotite- and amphibole-rich ultramafic rock in the area at the contact with tonalitic orthogneiss. (b) Harzburgite. Less-eroded rounded-shaped spots are orthopyroxene. (c) Amphibole-bearing olivine orthopyroxenite (some amphiboles are marked by black arrows). Orthopyroxenes (OPX) are indicated by yellow arrows. (d) Outcrop of the studied titanite-bearing dunite. Note its smooth surface compared to other outcrops.

## 2.2. Sample Description

In general, serpentinization of ultramafic rocks in the Ulamertoq body is very limited but commonly observed along the grain boundaries of olivine. Orthopyroxene sometimes occurs as poikilitic grains including olivines or fine-grained aggregates, particularly when its modal abundance is relatively high. Orthopyroxene is partially replaced by talc. Chlorite is often observed around spinel.

The studied titanian clinohumite-bearing peridotite is a medium-grained chlorite-bearing dunite with equigranular texture (Figure 3a,b). Orthopyroxene occurs as discrete grain in the studied dunite. Modal abundances of orthopyroxene and spinel modes are 2–4 vol.% and 1–2 vol.%, respectively, based on image processing from X-ray intensity maps (Figure 3c). Occurrence of some minerals as fine grains coupled with edge effect for X-ray intensity maps may cause some uncertainties in the mode estimation. During the image analyses, chlorite and titanian clinohumite modes were ignored because of their very fine grain size and low modal abundances (<1 vol.%). Olivine grains are classified into two types: (1) dusty olivine, which is characterized by many opaque mineral inclusions, and (2) clear olivine, which is free of opaque mineral inclusions (Figure 4). The clear olivines (usually <1 mm) are smaller than the dusty olivines (>1 mm). It is commonly observed that olivine grains with dusty cores have clear margins/rims (Figure 4a,e,f). Opaque mineral inclusions in the dusty olivines are mainly magnetite. Ilmenite is locally observed in olivine grains that are in contact with titanian clinohumite (Figure 4f). Dusty olivine is also commonly observed in other peridotites from the Ulamertoq body [40]. Orthopyroxene has a finer grain size (200  $\mu\text{m}$  in average) compared to olivine and is uniformly distributed (Figure 3c). Talc occurs locally around orthopyroxenes. Dark-colored spinels, mainly ferrichromite-magnetite (<300  $\mu\text{m}$ ), are always associated with chlorite (Figures 3 and 4). Titanian clinohumite is distinguished by its yellow color using optical microscopy under plane-polarized light and occurs as disseminated discrete grains. It is worth noting that a titanian clinohumite grain is directly in contact with olivine and chlorite in Figure 4d. Carbonate grains are present and are in contact with olivine and titanian clinohumite (Figure 4e,f). Carbonate minerals are mainly calcium carbonate (not shown in tables).

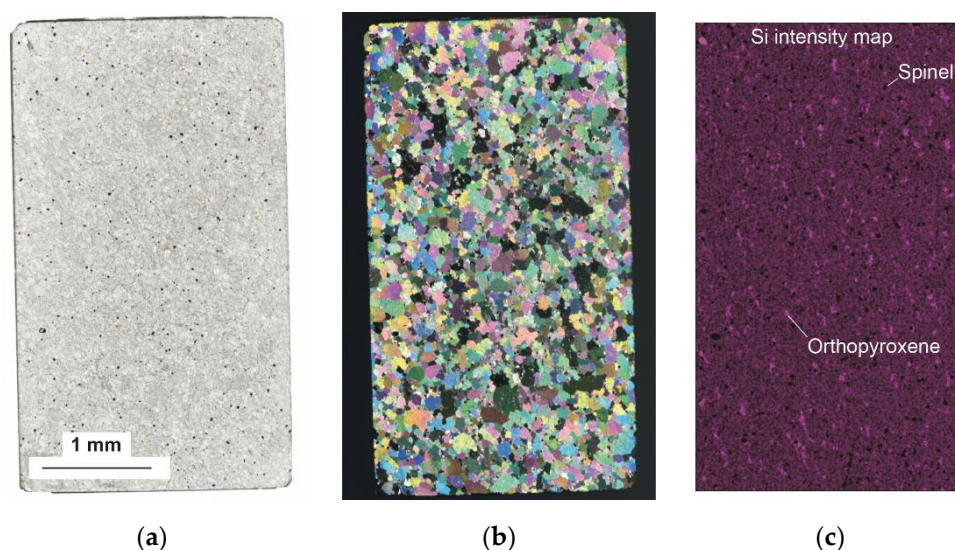


**Figure 3.** Thin section images of titanian clinohumite-bearing peridotite from the Ulamertoq ultramafic body. (a) Plane-polarized light image with black-colored small phases which are mainly spinel; (b) Cross polarized light image of (a); (c) Si intensity map of (a). Dark, small phases are spinel, bright small phases are orthopyroxene, and other phases are mainly olivine.

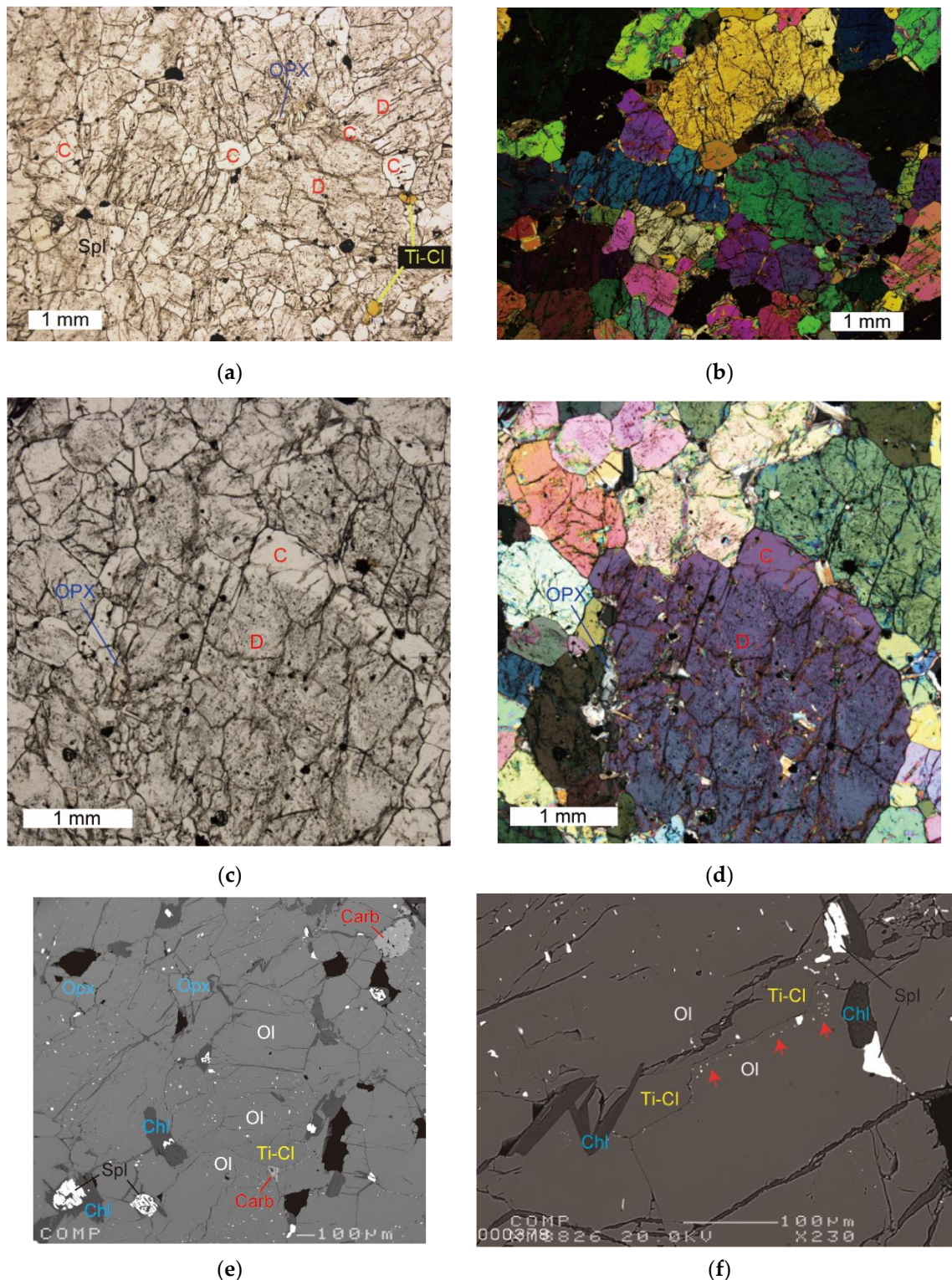


**Figure 4.** Photomicrographs and back-scattered electron images of the titanian clinohumite-bearing peridotite from the Ulamertoq ultramafic body. (a) Discrete grains of dusty and clear olivine. Plane-polarized light image. C = Clear olivine, D = Dusty olivine, OPX = orthopyroxene, Spl = spinel, Ti-Cl = Titanian clinohumite; (b) Cross polarized light image of (a); (c) Dusty olivine (D) with clear rim (C); (d) Cross polarized light image of (c); (e) Back-scattered electron image of magnetite inclusions in dusty olivines; (f) Back-scattered electron image of titanian clinohumite (Ti-Cl) and other minerals. Fine-grains of ilmenite and magnetite are aligned with olivine around the titanian clinohumite grain (red arrows). Dark phases are chlorite (Chl). Ol = olivine, Spl = spinel.

### 2.3. Analytical Methods

Major-element compositions of minerals were determined using an electron probe micro-analyzer (EPMA) (JEOL JXA-8800 Superprobe, JEOL Ltd., Akishima, Toyko, Japan) at Kanazawa University. The analyses were performed with an accelerating voltage of 20 kV and beam current of 20 nA, using a 3  $\mu\text{m}$  beam diameter. Natural and synthetic mineral standards were used for calibration and JEOL software using ZAF corrections is applied for data reduction. In-house mineral standards (olivine, chromian spinel, diopside and K-feldspar) were measured repeatedly to monitor data quality. The measured concentrations in these minerals are consistent with the averaged values from long-term analyses within 1  $\sigma$  standard deviation for all the elements. Data precision, which is established by multiple analyses of one point in the house-prepared standard minerals, is better than 5% and 10% relative standard deviation from the averaged values for elements with abundances > 0.5 wt.% and <0.5 wt.%, respectively. Details of EPMA are given in [41,42]. Major element compositions of minerals are shown in Tables 1–5.

**Table 1.** Major element compositions of olivine from the representative samples from Ulamertoq peridotite body.

wt.%	SiO <sub>2</sub>	FeO*	MnO	MgO	NiO	Total	Si	Fe*	Mn	Mg	Ni	Total	Fo
<b>Dusty</b>													
Grain1	40.9	6.8	0.2	51.6	0.4	99.9	0.993	0.137	0.003	1.866	0.007	3.007	93.1
Grain1	40.9	7.1	0.1	51.8	0.4	100.3	0.990	0.144	0.003	1.866	0.007	3.010	92.9
Grain2	41.5	6.7	0.2	52.5	0.4	101.3	0.993	0.134	0.003	1.869	0.007	3.007	93.3
Grain2	41.1	7.1	0.1	52.4	0.4	101.1	0.987	0.142	0.003	1.874	0.008	3.013	93.0
Grain3	41.1	6.9	0.1	51.7	0.4	100.3	0.994	0.139	0.003	1.862	0.008	3.006	93.1
Grain3	41.0	6.7	0.1	51.2	0.4	99.3	0.999	0.135	0.002	1.857	0.008	3.001	93.2
Grain9	41.2	7.1	0.1	52.3	0.4	101.1	0.989	0.142	0.003	1.869	0.007	3.010	93.0
Grain9	41.5	6.8	0.2	52.5	0.4	101.4	0.992	0.135	0.003	1.869	0.008	3.008	93.3
Grain10/1	41.0	6.9	0.1	51.7	0.4	100.3	0.991	0.139	0.002	1.862	0.007	3.001	93.1
Grain10/1	40.8	6.7	0.1	51.5	0.4	99.5	0.993	0.137	0.003	1.867	0.008	3.007	93.2
Grain11/1	41.0	6.6	0.1	51.2	0.4	99.3	0.998	0.135	0.003	1.858	0.008	3.001	93.2
Grain12/1	40.7	6.8	0.1	52.7	0.4	100.7	0.981	0.137	0.003	1.892	0.008	3.019	93.3
Grain13	40.8	6.8	0.1	50.2	0.4	98.3	1.004	0.140	0.003	1.841	0.008	2.996	92.9
Grain13	41.4	6.9	0.1	51.5	0.4	100.3	1.000	0.139	0.002	1.851	0.008	3.000	93.0
Grain14	41.1	7.0	0.1	51.3	0.4	100.0	0.996	0.141	0.003	1.854	0.008	3.003	92.9
Grain20/1	41.3	6.9	0.1	51.5	0.4	100.2	0.998	0.140	0.002	1.854	0.008	3.002	93.0
Grain20/1	41.0	7.2	0.1	51.6	0.4	100.3	0.993	0.145	0.002	1.859	0.007	3.007	92.8
<b>Dusty Low-NiO</b>													
Grain15	40.8	7.0	0.12	51.0	0.12	99.0	1.00	0.14	0.00	1.86	0.00	3.00	92.8
<b>Clear</b>													
Grain1	40.7	7.3	0.11	51.6	0.37	100.1	0.99	0.15	0.00	1.87	0.01	3.01	92.7
Grain1	40.7	7.1	0.13	51.7	0.39	100.0	0.99	0.14	0.00	1.87	0.01	3.01	92.9
Grain1	40.8	7.1	0.10	51.8	0.41	100.2	0.99	0.14	0.00	1.87	0.01	3.01	92.8
Grain1	41.1	6.7	0.13	52.1	0.45	100.5	0.99	0.14	0.00	1.87	0.01	3.01	93.3
Grain5	41.3	6.8	0.07	51.7	0.42	100.3	1.00	0.14	0.00	1.86	0.01	3.00	93.1
Grain7	41.1	7.3	0.14	52.0	0.37	100.9	0.99	0.15	0.00	1.86	0.01	3.01	92.7
Grain10/2	40.2	7.3	0.14	52.4	0.39	100.5	0.98	0.15	0.00	1.89	0.01	3.02	92.8
Grain11/2	41.3	7.3	0.12	51.9	0.40	100.9	0.99	0.15	0.00	1.86	0.01	3.01	92.7
Grain11/2	40.9	7.1	0.11	50.9	0.41	99.4	1.00	0.14	0.00	1.85	0.01	3.00	92.8

Table 1. Cont.

wt.%	SiO <sub>2</sub>	FeO*	MnO	MgO	NiO	Total	Si	Fe*	Mn	Mg	Ni	Total	Fo
Grain12/1	40.8	7.2	0.10	51.8	0.38	100.3	0.99	0.15	0.00	1.87	0.01	3.01	92.7
Grain13/2	41.1	7.1	0.15	51.6	0.40	100.4	0.99	0.14	0.00	1.86	0.01	3.01	92.8
Grain13/2	40.9	7.2	0.14	50.9	0.40	99.6	1.00	0.15	0.00	1.85	0.01	3.00	92.6
Grain20/2	41.2	6.9	0.09	51.8	0.42	100.4	0.99	0.14	0.00	1.86	0.01	3.00	93.0

Detection limit of analyses is as follow: <0.04 wt.% for TiO<sub>2</sub>, <0.03 wt.% for Al<sub>2</sub>O<sub>3</sub>, <0.07 wt.% for Cr<sub>2</sub>O<sub>3</sub>, <0.03 wt.% for CaO, Na<sub>2</sub>O and K<sub>2</sub>O %. FeO\* and Fe\* = all Fe as Fe<sup>2+</sup>. Cations are calculated as total oxygen = 4. Fo = 100 Mg/(Mg + Fe) atomic ratio.

**Table 2.** Major element compositions of orthopyroxene from the representative samples from the Ulamertoq peridotite body.

wt.%	Grain9	Grain2	Grain2-2	Grain10	Grain11	Grain3	Grain20	Grain20	Grain7	Grain7
SiO <sub>2</sub>	56.9	57.3	56.9	57.0	57.2	57.5	57.2	57.2	56.9	56.8
TiO <sub>2</sub>	0.10	0.08	0.07	0.09	0.08	0.10	0.08	0.12	0.08	0.09
Al <sub>2</sub> O <sub>3</sub>	1.6	1.5	1.3	1.6	1.5	1.6	1.6	1.8	1.5	1.6
Cr <sub>2</sub> O <sub>3</sub>	0.16	0.16	0.19	0.17	0.20	0.19	0.20	0.22	0.22	0.22
FeO*	5.3	5.6	5.4	5.4	5.3	5.3	5.5	5.4	5.2	5.4
MnO	0.17	0.14	0.14	0.13	0.15	0.15	0.16	0.12	0.13	0.16
MgO	35.4	35.4	35.5	35.2	35.4	35.5	35.2	35.2	35.1	35.3
CaO	0.15	0.14	0.10	0.13	0.14	0.16	0.12	0.15	0.09	0.16
NiO	-	0.06	0.06	0.06	-	-	0.07	0.06	-	0.07
Total	99.9	100.3	99.7	99.7	99.9	100.6	100.1	100.2	99.2	99.8
Si	1.96	1.96	1.96	1.96	1.96	1.96	1.96	1.96	1.96	1.96
Ti	0.00	0.00	0.00	0.00	0.00	0.00	0.00	0.00	0.00	0.00
Al	0.07	0.06	0.05	0.06	0.06	0.06	0.06	0.07	0.06	0.07
Cr	0.00	0.00	0.01	0.00	0.01	0.00	0.01	0.01	0.01	0.01
Fe*	0.15	0.16	0.16	0.16	0.15	0.16	0.15	0.15	0.16	0.15
Mn	0.00	0.00	0.00	0.00	0.00	0.00	0.00	0.00	0.00	0.00
Mg	1.81	1.81	1.82	1.80	1.81	1.80	1.81	1.80	1.80	1.80
Ca	0.01	0.01	0.00	0.00	0.01	0.00	0.01	0.01	0.00	0.01
Ni	0.00	0.00	0.00	0.00	0.00	0.00	0.00	0.00	0.00	0.00
Total	4.01	4.01	4.01	4.00	4.00	4.00	4.00	4.00	4.00	4.00
X <sub>Mg</sub>	0.922	0.919	0.921	0.921	0.923	0.921	0.923	0.922	0.919	0.921
X <sub>Cr</sub>	0.061	0.067	0.085	0.067	0.082	0.067	0.082	0.073	0.079	0.076

Detection limit of analyses is as follow: <0.03 wt.% for Na<sub>2</sub>O and K<sub>2</sub>O%, and <0.05 wt.% for NiO. "-" indicates than detection limit of analyses. Cations are calculated as total oxygen = 6.

The rare earth element (REE) and trace element (Li, Ti, Sr, Y, Zr, and Nb) compositions of orthopyroxene and titanian clinohumite are determined by 193 nm ArF Excimer laser ablation-inductively coupled plasma-mass spectrometry (LA-ICP-MS) at Kanazawa University (Agilent 7500S equipped with MicroLas GeoLas Q-plus). Orthopyroxene and titanian clinohumite were analyzed by ablating 100 µm and 60 µm spot diameters at 8 Hz, respectively, because of the size of analyzed minerals. The NIST SRM 612 standard was used as the primary calibration standard and is analyzed at the beginning of each batch of <8 unknowns, with a linear drift correction applied between each calibration. The element concentrations of NIST SRM 612 standard for the calibration are selected from the preferred values of [43]. Data reduction is facilitated using <sup>29</sup>Si as internal standard, based on Si contents obtained by EPMA following a protocol essentially identical to that outlined by [44]. NIST SRM 614, which is a synthetic silicate glass with a nominal concentration of 1 ppm for 61 elements including REEs, was analyzed for quality control during measurement. The measured concentrations in NIST SRM 614 glass are consistent with previously reported values to within 10% relative, and the data precision is better than 10% relative standard deviation for all the analytical elements. Details of the analytical method and data quality control are given in [45]. Representative trace-element compositions of orthopyroxenes and titanian clinohumite are shown in Table 6.

**Table 3.** Major element compositions of titanian clinohumite from the representative samples from Ulamertoq peridotite body.

	Grain 1	Grain 2-1	Grain 2-2	Grain 2-2	Grain 2-2	Grain 3	Grain 3									
wt. %	margin	margin	margin	margin	margin	rim	margin	core	margin	rim	rim	core	rim	margin	margin	margin
SiO <sub>2</sub>	37.6	37.3	36.8	37.0	37.5	37.9	37.4	38.2	37.2	37.6	37.9	37.2	37.4	36.5	37.0	36.8
TiO <sub>2</sub>	2.3	2.4	2.4	2.4	2.1	2.2	2.1	1.7	2.2	2.0	1.9	2.0	1.9	2.2	2.1	2.2
FeO*	5.4	5.4	5.2	5.3	5.4	5.1	5.3	5.6	5.2	5.4	5.3	5.4	5.3	5.5	5.4	5.3
MnO	0.1	0.1	0.1	0.1	0.1	0.1	0.1	0.1	0.1	0.1	0.1	0.1	0.1	0.1	0.1	0.1
MgO	51.7	52.1	51.9	52.0	51.5	52.4	52.2	51.6	52.1	51.7	51.6	52.4	51.4	51.9	52.5	52.3
NiO	0.3	0.2	0.3	0.3	0.3	0.2	0.3	0.3	0.3	0.3	0.2	0.3	0.2	0.3	0.2	0.3
F	2.3	2.2	2.1	2.2	2.1	2.2	2.4	1.6	2.0	1.7	1.5	2.1	2.0	2.1	2.1	2.0
H <sub>2</sub> O	1.7	1.8	1.8	1.7	1.8	1.8	1.6	2.0	1.8	2.0	2.1	1.8	1.8	1.8	1.8	1.8
O = F	1.0	0.9	0.9	0.9	0.9	0.9	1.0	0.7	0.8	0.7	0.7	0.9	0.8	0.9	0.9	0.8
Total	100.3	100.5	99.7	100.1	99.9	101.0	100.4	100.4	100.1	100.0	100.0	100.4	99.4	99.5	100.3	100.0
Si	4.03	3.99	3.97	3.98	4.04	4.03	4.00	4.09	3.99	4.04	3.98	4.05	3.95	3.95	3.95	4.08
Ti	0.19	0.19	0.19	0.19	0.17	0.17	0.17	0.14	0.18	0.16	0.16	0.15	0.17	0.18	0.18	0.15
Fe	0.48	0.49	0.47	0.48	0.49	0.46	0.48	0.50	0.47	0.49	0.48	0.48	0.48	0.48	0.49	0.48
Mn	0.01	0.01	0.01	0.01	0.01	0.01	0.01	0.01	0.01	0.01	0.01	0.01	0.01	0.01	0.01	0.01
Mg	8.26	8.31	8.33	8.32	8.26	8.31	8.33	8.24	8.33	8.28	8.35	8.29	8.37	8.36	8.35	8.27
Ni	0.03	0.02	0.02	0.02	0.02	0.02	0.02	0.02	0.02	0.02	0.02	0.02	0.02	0.02	0.02	0.02
Total	13.00	13.00	13.00	13.00	13.00	13.00	13.00	13.00	13.00	13.00	13.00	13.00	13.00	13.00	13.00	13.00
X <sub>Mg</sub>	0.941	0.942	0.943	0.942	0.941	0.945	0.943	0.940	0.944	0.941	0.943	0.942	0.942	0.941	0.943	0.942
X <sub>F</sub>	0.39	0.37	0.35	0.38	0.36	0.37	0.41	0.27	0.34	0.28	0.26	0.35	0.34	0.36	0.35	0.34
M	8.78	8.82	8.84	8.83	8.78	8.80	8.83	8.77	8.83	8.80	8.77	8.86	8.80	8.87	8.88	8.87
M/Si	2.18	2.21	2.23	2.22	2.17	2.18	2.21	2.14	2.21	2.18	2.15	2.23	2.17	2.25	2.25	2.25

Detection limit of analyses is as follow: <0.03 wt.% for Al<sub>2</sub>O<sub>3</sub>, CaO, Na<sub>2</sub>O and K<sub>2</sub>O%, and <0.07 wt.% for Cr<sub>2</sub>O<sub>3</sub>. Cation is calculated as total oxygen = 17. All Fe is treated as FeO. H<sub>2</sub>O is calculated on the basis of F and Ti contents and the exchange between Ti<sub>x</sub>O<sub>2x</sub>M<sub>1-x</sub>(OH)<sub>2-2x</sub> after the cation total is normalized to 13.

**Table 4.** Major element compositions of spinel from the representative samples from Ulamertoq peridotite body.

	Grain9-1	Grain9-2	Grain5	Grain1	Grain10	Grain12	Grain4	Grain4	Grain20	Grain13	Grain7-1	Grain7-2	Grain7-3
wt. %	core	core	in ol	core	core	core	core	rim	core	core	core	core	core
TiO <sub>2</sub>	<0.04	0.30	0.32	0.33	0.26	1.33	0.09	0.33	0.23	0.47	0.34	0.32	0.22
Al <sub>2</sub> O <sub>3</sub>	0.07	2.34	0.31	3.08	8.76	6.55	26.76	9.92	4.14	2.15	2.53	3.49	2.18
Cr <sub>2</sub> O <sub>3</sub>	6.2	38.9	21.2	45.2	38.9	29.1	34.4	39.6	36.8	41.0	42.0	42.6	30.5
FeO*	85.6	51.1	70.2	43.5	43.4	55.3	27.1	42.6	53.0	48.9	48.0	45.9	59.1
MnO	0.04	0.64	0.40	0.69	0.60	0.42	0.30	0.51	0.53	0.71	0.62	0.74	0.45
MgO	0.7	3.1	2.4	3.5	5.0	4.0	11.2	5.8	3.4	3.1	3.6	4.1	2.6
NiO	0.37	0.16	0.61	0.14	0.29	0.47	0.12	0.29	0.25	0.26	0.14	0.10	0.28
Total	93.1	96.6	95.4	96.5	97.2	97.2	100.0	99.1	98.3	96.7	97.1	97.4	95.4
Ti	-	0.01	0.01	0.01	0.01	0.04	0.00	0.01	0.01	0.01	0.01	0.01	0.01
Al	0.00	0.10	0.01	0.13	0.36	0.27	0.96	0.40	0.17	0.09	0.11	0.15	0.10
Cr	0.19	1.13	0.62	1.31	1.08	0.81	0.83	1.07	1.04	1.19	1.21	1.21	0.90
Fe <sup>3+</sup>	1.80	0.75	1.34	0.53	0.54	0.86	0.20	0.51	0.77	0.68	0.66	0.61	0.99
Fe <sup>2+</sup>	0.95	0.82	0.86	0.80	0.73	0.77	0.49	0.70	0.81	0.82	0.80	0.77	0.85
Mn	0.00	0.02	0.01	0.02	0.02	0.01	0.01	0.01	0.02	0.02	0.02	0.02	0.01
Mg	0.04	0.17	0.13	0.19	0.26	0.21	0.51	0.30	0.18	0.17	0.19	0.22	0.15
Ni	0.01	0.00	0.02	0.00	0.01	0.01	0.00	0.01	0.01	0.01	0.00	0.00	0.01
Total	3.00	3.00	3.00	3.01	3.00	2.99	3.00	3.00	3.00	3.00	3.00	3.00	3.00
X <sub>Mg</sub>	0.043	0.170	0.135	0.194	0.262	0.215	0.509	0.297	0.181	0.172	0.194	0.223	0.147
X <sub>Cr</sub>	0.984	0.918	0.979	0.908	0.748	0.749	0.463	0.728	0.856	0.928	0.917	0.891	0.904
Y <sub>Cr</sub>	0.094	0.572	0.316	0.664	0.544	0.418	0.416	0.539	0.524	0.606	0.611	0.615	0.452
Y <sub>Al</sub>	0.002	0.051	0.007	0.067	0.183	0.140	0.483	0.201	0.088	0.047	0.055	0.075	0.048
Y <sub>Fe<sup>3+</sup></sub>	0.904	0.377	0.677	0.269	0.273	0.442	0.101	0.260	0.388	0.347	0.333	0.310	0.499

Detection limit of analyses is as follows: <0.03 wt.% for SiO<sub>2</sub>, CaO, Na<sub>2</sub>O and K<sub>2</sub>O. Cation is calculated as total oxygen = 4. Fe<sub>2</sub>O<sub>3</sub> and FeO are calculated based on stoichiometry. X<sub>Mg</sub> = Mg/(Mg + Fe<sup>2+</sup>), X<sub>Cr</sub> = Cr/(Cr + Al), Y<sub>Cr</sub> = Cr/(Cr + Al + Fe<sup>3+</sup>), Y<sub>Al</sub> = Al/(Cr + Al + Fe<sup>3+</sup>), Y<sub>Fe<sup>3+</sup></sub> = Fe<sup>3+</sup>/(Cr + Al + Fe<sup>3+</sup>).

**Table 5.** Major element compositions of chlorite from the representative samples from Ulamertoq peridotite body.

wt.%	Grain1/2	Grain1	Grain1	Grain2	Grain3
SiO <sub>2</sub>	32.1	31.6	31.5	32.3	30.8
TiO <sub>2</sub>	<0.04	0.09	0.06	<0.04	0.06
Al <sub>2</sub> O <sub>3</sub>	17.4	17.3	17.4	15.7	17.2
Cr <sub>2</sub> O <sub>3</sub>	1.6	1.7	1.7	1.9	1.6
FeO	2.2	2.5	2.5	2.5	2.5
MgO	32.6	32.5	32.2	33.0	32.3
NiO	0.21	0.21	0.21	0.21	0.2
Total	86.1	85.8	85.5	85.6	84.8
F wt.%	0.12	0.15	0.35	0.18	0.36
Si	2.83	2.81	2.80	2.87	2.77
Ti	-	0.01	0.00	-	0.00
Al	1.81	1.80	1.82	1.65	1.82
Cr	0.11	0.12	0.12	0.13	0.12
Fe	0.16	0.18	0.18	0.19	0.19
Mg	4.28	4.29	4.27	4.38	4.33
Ni	0.01	0.02	0.02	0.01	0.01
Total	9.21	9.23	9.22	9.24	9.26
X <sub>Mg</sub>	0.964	0.959	0.959	0.959	0.958
X <sub>Cr</sub>	0.058	0.062	0.062	0.073	0.06

Detection limit of analyses is as follow: <0.07 wt.% for MnO, and <0.03 wt.% for CaO, Na<sub>2</sub>O and K<sub>2</sub>O%. All Fe is treated as Fe<sup>2+</sup>. Cation is calculated as total oxygen = 13. X<sub>Mg</sub> = Mg/(Mg + Fe) atomic ratio, X<sub>Cr</sub> = Cr/(Cr + Al) atomic ratio.

**Table 6.** Trace element compositions of orthopyroxene and titanian clinohumite.

ppm	OPX			DL for 100	Ti Clinohumite			DL for 60
Li	8.4	7.6	8.7	0.1	13	9	7	0.6
B	3.3	2.1	3.3	0.2	14	8	11	1.0
Sc	30.98	34.38	33.49	0.03	6	8	7	0.1
Ti	438	478	444	0.1	10,930	11,253	7866	0.2
V	74	73	74	0.02	26	32	19	0.1
Cr	1771	1738	1722	0.6	77	81	53	1.9
Co	44	43	43	0.006	127	121	129	0.0
Ni	497	475	497	0.3	2552	2423	2733	0.7
Rb	<	<	<	0.008	<	<	<	0.029
Sr	0.005	0.005	0.010	0.002	0.097	0.095	0.101	0.007
Y	1.87	2.23	1.92	0.002	0.023	0.074	0.418	0.004
Zr	0.73	0.74	0.58	0.004	1.663	1.721	0.987	0.007
Nb	0.016	0.018	0.020	0.002	6.649	7.100	5.038	0.000
Cs	<	<	<	0.005	<	<	<	0.017
Ba	<	<	<	0.011	<	<	0.053	0.033
La	<	0.002	0.004	0.001	<	0.020	0.161	0.004
Ce	0.008	0.009	0.015	0.001	<	0.076	0.439	0.004
Pr	0.002	0.003	0.002	0.001	<	0.008	0.043	0.004
Nd	0.021	0.022	0.019	0.006	<	0.042	0.173	0.019
Sm	0.022	0.025	0.017	0.004	<	<	0.033	0.017
Eu	0.003	0.003	0.003	0.003	<	<	<	0.004
Gd	0.065	0.071	0.048	0.008	<	<	0.041	0.024
Tb	0.020	0.021	0.017	0.002	<	<	<	0.005
Dy	0.229	0.270	0.228	0.004	<	<	0.052	0.016
Ho	0.067	0.083	0.070	0.002	<	<	0.017	0.007
Er	0.299	0.357	0.321	0.005	<	<	0.060	0.011
Tm	0.055	0.066	0.060	0.002	<	0.002	0.011	0.006
Yb	0.468	0.530	0.496	0.007	0.019	0.033	0.084	0.015
Lu	0.072	0.086	0.079	0.002	0.007	0.009	0.014	0.005
Hf	0.071	0.072	0.061	0.007	0.035	0.048	0.026	0.024
Ta	<	<	<	0.002	0.155	0.184	0.133	0.004
Pb	0.059	0.013	0.044	0.011	0.090	0.071	0.074	0.028
Th	<	<	<	0.004	<	<	0.043	0.015
U	<	<	<	0.004	0.041	0.017	0.071	0.008

"<" indicates lower than detection limit, OPX = orthopyroxene, DL = detection limit of analyses, Ti Clinohumite = Titanian clinohumite.

### 3. Results

The forsterite ( $=100 \text{ Mg}/(\text{Mg} + \text{Fe}^{2+})$  atomic ratio), NiO and MnO contents of olivine are  $93.0 \pm 0.2$ ,  $0.40 \pm 0.02$  wt.% and  $0.13 \pm 0.02$  wt.% for the dusty olivine, and  $92.8 \pm 0.2$ ,  $0.40 \pm 0.02$  wt.% and  $0.11 \pm 0.02$  wt.% for the clear olivine, respectively, except for one analytical point with 0.1 wt.% of NiO content for a dusty olivine (Figure 5). The clear olivine is likely lower in Fo value than the dusty olivine, but they are identical within 1 sigma variations.

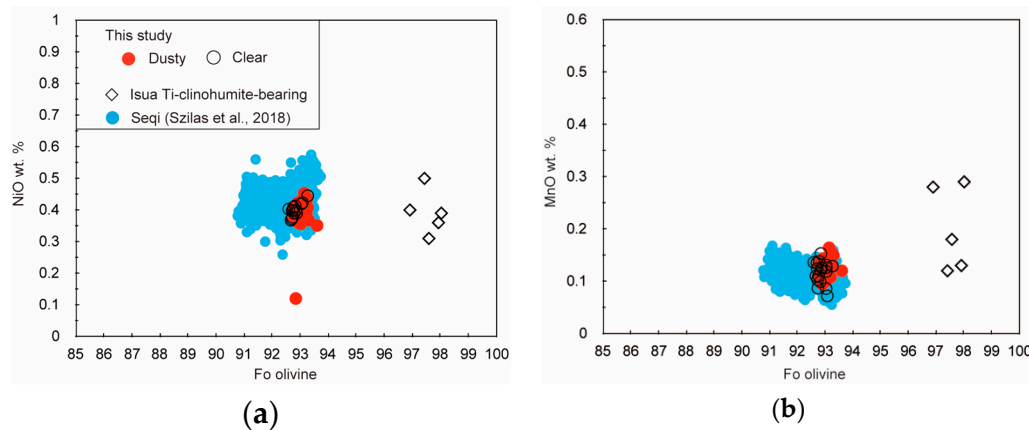


**Figure 5.** Olivine compositions. (a) Relationships between the Fo content and NiO; (b) the Fo content and MnO. Olivines from the titanian clinohumite-bearing peridotites from the Isua Supracrustal Belt are from [12,24].

$X_{\text{Mg}}$  ( $=\text{Mg}/(\text{Mg} + \text{Fe}^{2+})$  atomic ratio) of orthopyroxene is 0.92. The  $\text{Al}_2\text{O}_3$  and  $\text{Cr}_2\text{O}_3$  contents of orthopyroxenes are 1.3–1.8 wt.% and around 0.2 wt.%, respectively, resulting in low  $X_{\text{Cr}}$  ( $=\text{Cr}/(\text{Cr} + \text{Al})$  atomic ratio) (Figure 6). The  $\text{TiO}_2$  and CaO contents of orthopyroxene are  $<0.12$  wt.% and  $<0.2$  wt.%. Chondrite-normalized REE patterns for orthopyroxenes show an abrupt decrease from heavy rare earth elements (HREEs) to light REEs, exhibiting negative Eu anomalies (Figure 7a). Primitive mantle-normalized trace element patterns of orthopyroxene show negative anomalies of Eu as well as Sr, and positive anomalies of HFSEs, such as Ti, Zr, and Nb (Figure 7b).

The  $\text{TiO}_2$  and F contents of titanian clinohumite are 1.6–2.4 wt.% and 1.7–2.4 wt.%, respectively (Figure 8). Trace element compositions of titanian clinohumites are variable, but are characterized by low middle REEs and LILEs, but high HFSEs, such as Ti, Zr, and Nb (Figure 9).

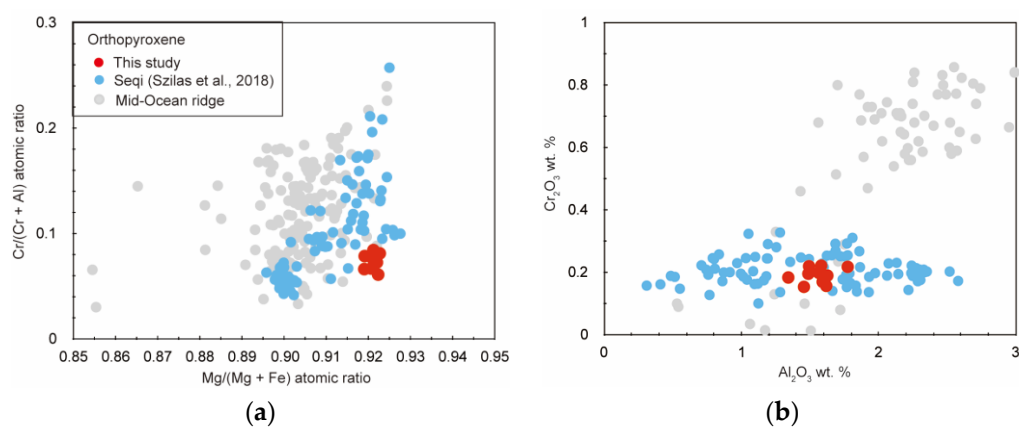


**Figure 6.** Major element composition of orthopyroxene. (a) Relationships between  $\text{Mg}/(\text{Mg} + \text{Fe}^{2+})$  atomic ratio and  $\text{Cr}/(\text{Cr} + \text{Al})$  atomic ratio; (b) Relationships between  $\text{Al}_2\text{O}_3$  wt.% and  $\text{Cr}_2\text{O}_3$  wt.%. Data for abyssal peridotites recovered from mid-ocean ridges are from [46].

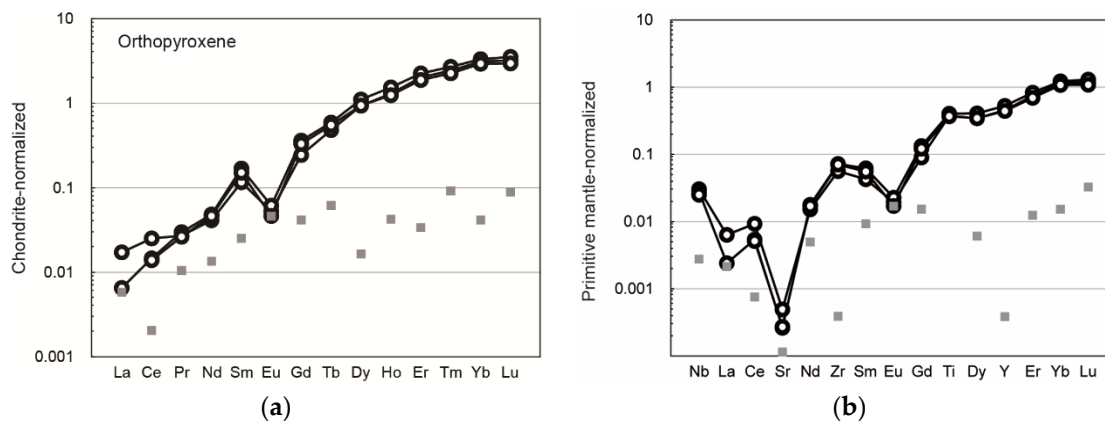


**Figure 7.** Trace element composition of orthopyroxene. (a) Chondrite-normalized rare earth element patterns; (b) Primitive mantle-normalized trace element patterns. Gray squares indicate values for the detection limits.

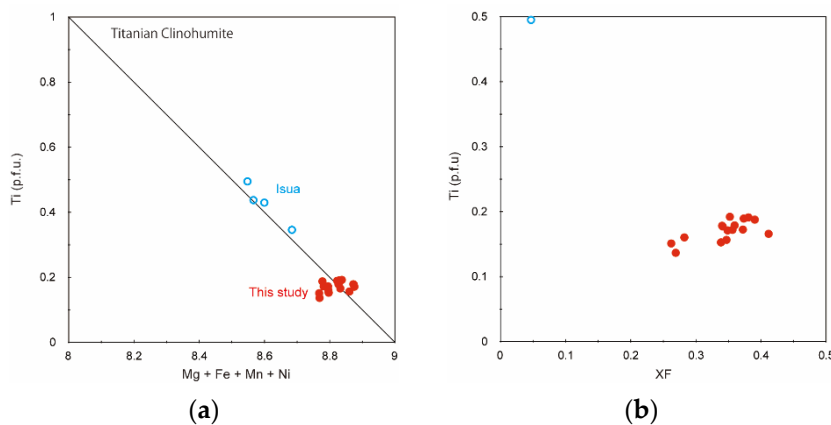


**Figure 8.** Major element compositions of titanian clinohumite. (a) Relationships between metals ( $Mg + Fe + Mn + Ni = M$ ) and Ti; (b) Relationships between Ti and  $X_F$ . Titanian clinohumites from the Isua are from [12,24].

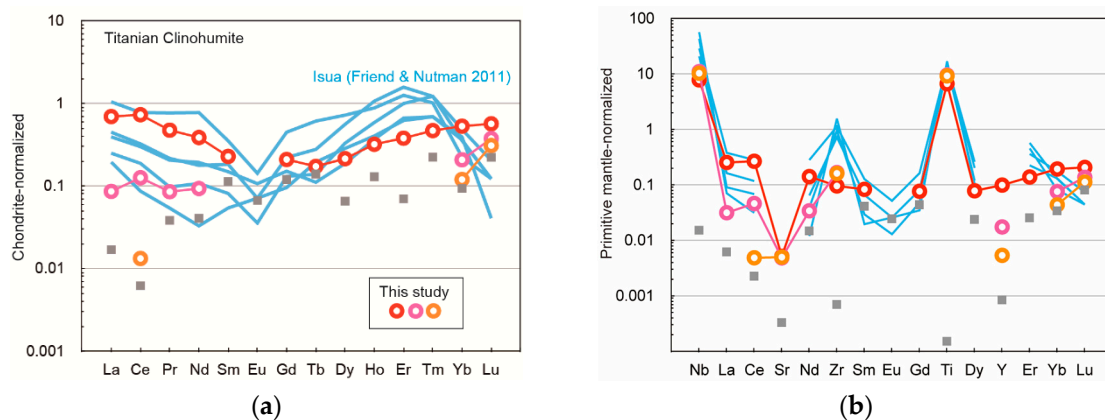


**Figure 9.** Trace element composition of titanian clinohumites. (a) Chondrite-normalized rare earth element patterns; (b) Primitive mantle-normalized trace element patterns. Data from the Isua peridotites are from [12]. Gray squares indicate values for the detection limits.

Spinel group minerals are high in  $Fe^{3+}$ , mainly ferrichromite, chromemagnetite to magnetite, except for one ferrialuminochromite (Figure 9). The  $TiO_2$  content of spinels are generally lower than 0.5 wt.%, except for analytical point of 1.4 wt.% (Figure 10).

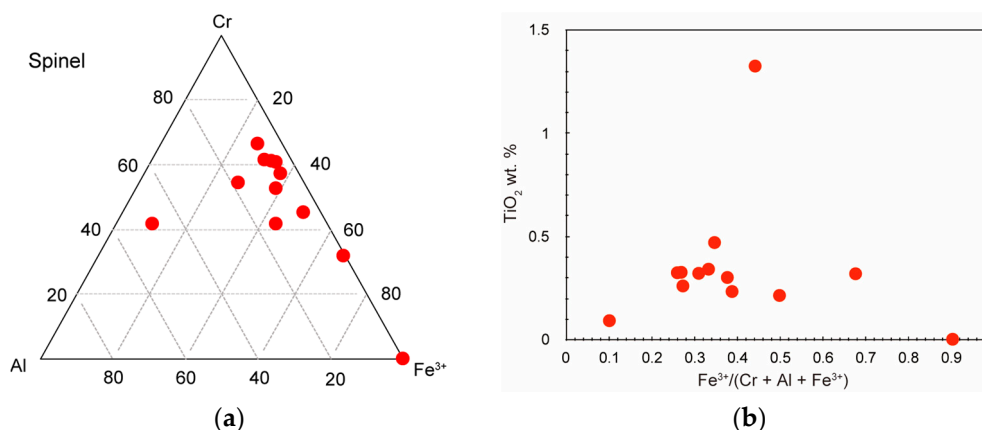


**Figure 10.** Spinel composition. (a) Ternary cation diagram; (b) Relationships between  $\text{Fe}^{3+}/(\text{Cr} + \text{Al} + \text{Fe}^{3+})$  and  $\text{TiO}_2$  wt.%.

Chlorite is chromian (1.6–1.9 wt.% for  $\text{Cr}_2\text{O}_3$ ,  $X_{\text{Cr}} = 0.06$ –0.07), and their F contents of chlorite is <0.4 wt.%.

## 4. Discussion

### 4.1. Pressure-Temperature Conditions for the Titanian Clinohumite-Bearing Peridotite

No garnet, including potential relics, has been observed in peridotites from the Ulamertoq ultramafic body, which indicates pressures lower than about 2 GPa during its (re-)crystallization. This is consistent with the lack of Ti-chondrodite, which also belongs to the humite group minerals, in the Ulamertoq samples. Ti-chondrodite is stable at higher pressure conditions (2 GPa) than Ti-clinohumite in a peridotite system [31,47,48]. Partial substitution of fluorine for OH in titanian clinohumite and substitution of Cr for Al in chlorite stabilize these hydrous minerals at higher temperature conditions compared to F-free clinohumite and Cr-free chlorite [20,29,35,49–51]. Evans and Trommsdorff [35] suggested that fluorine-rich compositions are probably critical for the stability of clinohumite from the garnet-peridotite stability field down to amphibolite facies conditions.

In Figure 11, the stability reactions for an F-free and F-bearing titanian clinohumites, and divariant fields for titanian clinohumite, olivine, and ilmenite are shown in grey-colored areas. The presence of tiny ilmenites (+magnetites) in olivine adjacent to titanian clinohumite in the studied sample suggests that part of the titanian clinohumite was decomposed by the reaction: titanian clinohumite = olivine + ilmenite + fluid. The divariant field for titanian clinohumite with  $X_{\text{F}} = 0.4$ , olivine and ilmenite, shown as the orange-colored area, is located at temperature lower than 900 °C and pressure of 0.5–2.0 GPa (Figure 11). At this pressure condition, chromian chlorite would be stable together with olivine and orthopyroxene (dark orange-colored area of Figure 11). Therefore, the temperature conditions for the coexisting F ( $X_{\text{F}} = 0.3$ –0.4)-bearing titanian clinohumite, and chromian chlorite in peridotite can be roughly estimated as around 800 °C (Figure 11). We note that this temperature is consistent with granulite facies metamorphism in the Akia Terrane (~820–850 °C under 0.8–1 GPa), which likely occurred in the period 2857–2700 Ma [38] (Figure 11).

A calcium carbonate, found in contact with olivine, is the only Ca-rich phase in the studied sample. In peridotite- $\text{CO}_2$ - $\text{H}_2\text{O}$  systems, the stability and nature of carbonate minerals depends on pressure, temperature, and  $\text{CO}_2$  fugacity conditions. Orthopyroxene and dolomite are stable at pressure >2 GPa at 800 °C, whereas olivine, diopside, and  $\text{CO}_2$  are stable at lower pressure conditions [52–54]. Olivine and calcite are stable >500 °C at around 1–2 GPa in CaO-bearing system at reasonable  $\text{CO}_2$  fugacity conditions [54]. Olivine and calcite can coexist with F-poor titanian clinohumite at around 500 °C. However, the temperature conditions for the F ( $X_{\text{F}} = 0.3$ –0.4)-bearing titanian clinohumite formation in the studied peridotite were roughly estimated as around 800 °C. In addition, the minor occurrence of

carbonate minerals, and their texture indicates that carbonates might have formed during a late stage where calcium carbonate components infiltrated locally.

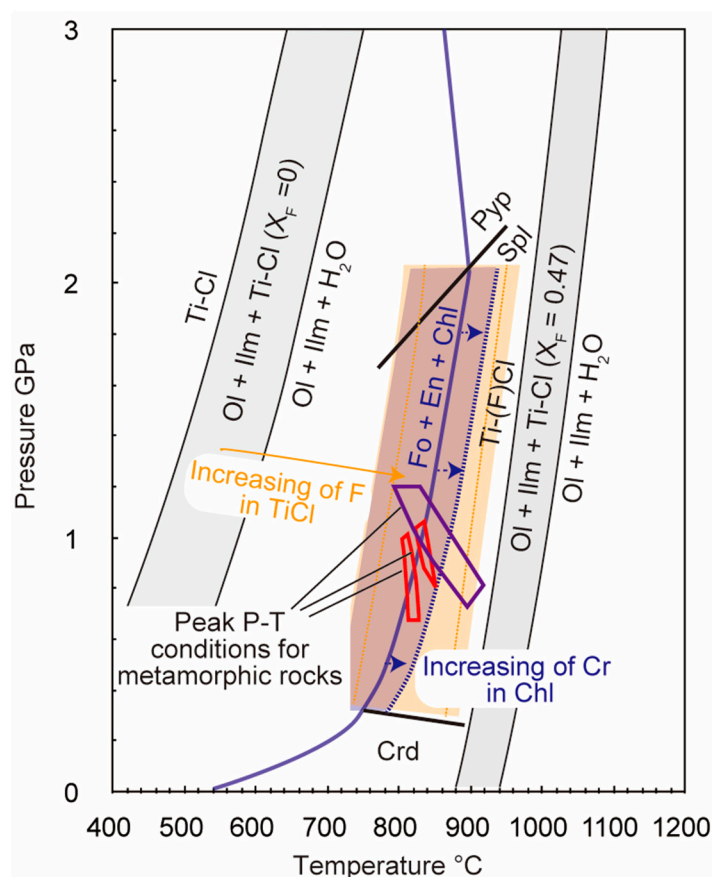


**Figure 11.** P-T conditions for the studied titanian clinohumite-bearing peridotite (light red field). The reaction curves of the F-free ( $X_F = 0$ ) titanian clinohumite ( $X_{Ti} = 0.28$ ,  $X_{Fe} = 0.04$ , where  $X_{Ti} = 2Ti/(2Ti + OH)$ ) and the F-bearing ( $X_F = 0.47$ ) one ( $X_{Ti} = 0.19$ ,  $X_{Fe} = 0.03$ ) after [51]. The divariant fields for the presence of titanian clinohumite, olivine, and ilmenite are shown as grey-colored fields the dashed and solid lines are for each clinohumite. The incorporation of Cr in chlorite expands its stability field (schematically shown as blue-colored dashed line with arrows towards increasing Cr) to higher temperature conditions. Chromium-free chlorite stability field are compiled by [55]. The peak P-T conditions estimated for metapelites and metabasite from the Akia terrane are shown as fields with red and violet outlines, respectively [38]. Pyp/Spl = the reaction from pyrope (Pyp) + olivine = enstatite + spinel (Spl), Chl = chlorite, Crd = cordierite stability field, En = enstatite, Fo = forsterite, Ilm = ilmenite, Ol = olivine, Ti-Cl = titanian clinohumite.

#### 4.2. Petrogenesis of the Studied Titanian Clinohumite-Bearing Ultramafic Rock

The studied peridotite is an orthopyroxene-bearing chlorite dunite. Orthopyroxene in the studied dunite plots at the highest  $X_{Mg}$  end of the compositional range of abyssal peridotites recovered from the mid-ocean ridges, whereas its  $X_{Cr}$  is almost at the lowest end (Figure 6). The  $Cr_2O_3$  content in orthopyroxene is generally low. Trace element patterns of orthopyroxene show negative anomalies of Sr and Eu (Figure 7), which suggest the role of plagioclase during (re-)crystallization of the studied ultramafic rocks. Also, the HREE contents of the Ulamertoq orthopyroxenes are considerably more enriched than those from residual peridotite [56]. The orthopyroxene composition, combined with the absence of clinopyroxene, indicates that the host harzburgite is not a simple residue after partial melting from primitive mantle compositions.

Orthopyroxene in the studied sample is geochemically characterized by being low in  $\text{Al}_2\text{O}_3$  and  $\text{Cr}_2\text{O}_3$ . Low- $\text{Al}_2\text{O}_3$  and  $\text{Cr}_2\text{O}_3$  orthopyroxenes are observed in deserpentinized peridotites [57–60]. It is noteworthy that magnetite inclusion-rich olivine, like the dusty olivine in this study, is commonly observed in deserpentinized peridotites. Some deserpentinized peridotites, in fact, contain titanian clinohumite and its derivative mineral assemblage that resulted from its breakdown [24,30,36]. Magnetite inclusions in olivine can be interpreted as remnants of former serpentinite after dehydration, probably under relatively high oxygen fugacity conditions. Several other mechanisms can also explain the origin of magnetite inclusions in olivine: oxidation of olivine and exsolution from ultra-high pressure olivine in decompression [61]. However, orthopyroxene inclusions associated with magnetite inclusions are absent, and the lack of evidence for ultra-high-pressure conditions in the studied sample makes oxidation or ultra-high-pressure decompression of olivine unlikely explanations. We suggest that dehydration of former serpentinites, under granulite-facies conditions, could explain the magnetite inclusions in the olivine. Dusty olivine is also commonly observed in the Seqi ultramafic body in the Akia Terrane [9], indicating that deserpentinized ultramafic rocks might occur in several ultramafic bodies in the Akia terrane. Szilas and colleagues [9] calculated pseudosections using PerpleX [62] for ultramafic rocks from the nearby Seqi ultramafic body. Their results suggest that the studied peridotites could be derived from lower grade serpentinitized peridotite during granulite facies metamorphic overprint. This scenario is certainly a possibility given the complex polymetamorphic evolution of the Akia Terrane [38].

Low- $\text{Al}_2\text{O}_3$  and  $\text{Cr}_2\text{O}_3$  orthopyroxenes are also reported from metasomatized peridotites by subducting slab-derived silica-rich metasomatic agents [25,63–65]. Iizuka and Nakamura [66] confirmed the formation of titanian clinohumite in an experimental simulation of slab-mantle interactions. The effect of metasomatism in the studied rocks can be deduced from field occurrences of phlogopite-amphibole-rich metasomatized ultramafic rocks and amphibole-bearing orthopyroxenite in the Ulamertoq body (Figure 2). Orthopyroxene in some Ulamertoq peridotites can occur as poikilitic and/or fine-grained aggregate, which is different from the typical textures of residual harzburgite. Although the studied samples come from a relatively small ultramafic body included in a large crustal domain (Figure 1), and from the field perspective have apparently no clear connection with a subducting environment, we suggest that further studies on the potential metasomatism of these rocks could be useful and should be conducted.

#### *4.3. Comparison with Titanian Clinohumite-Bearing Ultramafic Rock in the Isua Supracrustal Belt and Its Significance*

Titanian clinohumite-bearing peridotites were reported from the 3.8 Ga Isua Supracrustal Belt, which is part of the Itsaq Gneiss Complex [12,24]. Olivine grains with and without magnetite inclusions, which are similar to the dusty and clear olivines in the present study, are also reported in the Isua titanian clinohumite-bearing peridotites [24]. Dymek et al. [24] pointed out that the Isua peridotites are metamorphosed peridotites from the former serpentinites, followed by later serpentinitization. As we have discussed above, the titanian clinohumite-bearing dunite in our study is also likely formed by the dehydration of serpentinite. We suggest that the effects of hydration/dehydration processes should therefore be considered carefully in future studies on the origin of ultramafic bodies found within Archaean metamorphic terranes.

There are certain differences between the Ulamertoq and Isua titanian clinohumite-bearing peridotites, and especially the mineral compositions in the Isua titanian clinohumite-bearing ultramafic rocks, are not identical to those of the studied sample. The Fo content of olivine is higher in the Isua bodies than the Ulamertoq. Several factors likely contributed to the differences in the Fo content between these ultramafic bodies. The volume of magnetite grains in deserpentinized olivines can control the Fo content of olivines, because less magnetite results in olivine with lower Fo content, whereas abundant magnetite olivine increases Fo during subsolidus exchange [67]. The volume of chromite can also control the Fo content on cooling; samples with high chromite concentration have

higher Fo content. Varying iron content of the former serpentine is also an important controlling factor for the differences in the Fo content. Careful comparison of magnetite volumes within olivine between the Ulamertoq and the Isua bodies are required to fully evaluate the relationships to the corresponding Fo contents. The Isua titanian clinohumites have higher TiO<sub>2</sub> content and lower F contents than the Ulamertoq (Figures 5 and 8). Sánchez-Vizcaíno et al. [36] reported titanian clinohumite grains from a deserperentinized peridotite body in Cerro del Almirez, SE Spain, which show differences in the degree of dehydration. Their results suggest that OH-titanian clinohumite occurs in antigorite serpentinite whereas F-OH-titanian clinohumite is only observed in chlorite harzburgite. Antigorite serpentinite is not commonly observed in the Ulamertoq body, and it is possible that the Ulamertoq ultramafic body suffered from a high degree of deserperentinization from former serpentinites.

Another difference is the presence of titanian chondrodite in the Isua peridotite [12,24]. Experimental results and studies on natural samples suggest that the titanian chondrodite-bearing Isua peridotite is stable at higher pressure conditions than the studied titanian clinohumite-bearing dunite from Ulamertoq, and that the Isua rocks likely suffered ultra-high pressure conditions [31,47,48].

The tectonic settings of ultramafic rocks in the Archaean terranes of southern West Greenland are still not clear. The present study demonstrates that titanian clinohumite-bearing peridotites occur, at least locally in the Akia Terrane, and are thus distributed in several Archaean terranes in southern West Greenland. It is interesting to note that titanian clinohumite-bearing ultramafic rocks have been observed at the convergent plate margins, including (ultra-) high pressure metamorphic belts and subduction zones [30,32,36,48,68]. Polat et al. [69] compared the Mesozoic Suru orogenic belt, China, and the Supracrustal Belts in various Archaean terranes, and suggested that remarkable similarities exist between them. That study suggested that all lithological packages of the Archaean terranes of southern West Greenland are similar to those from the Mesozoic Suru orogenic belt, indicating that both Archaean ultramafic and crustal rocks were probably formed at convergent plate boundaries.

## 5. Conclusions

A titanian clinohumite-bearing chlorite dunite was found in the Ulamertoq ultramafic body of the 3.0 Ga Akia Terrane, southern West Greenland. Geochemical characteristics of the chlorite dunite host for titanian clinohumite do not fit residual peridotites after melt extraction from the primitive mantle. The titanian clinohumite is fluorine-bearing and has partly decomposed to ilmenite and olivine. This observation, coupled with the coexistence with chromian chlorite, indicates equilibration at around 800–900 °C under garnet-free conditions (<2 GPa), which is consistent with granulite facies metamorphic conditions reported from the Akia Terrane. The occurrence of magnetite inclusion-rich dusty olivines, together with pyroxene compositions in the studied titanian clinohumite-bearing peridotite, suggests a reaction involving deserperentinized peridotites from former serpentinites in the Ulamertoq ultramafic body. In light of our results, we suggest that the effects of hydration/dehydration processes, and their potential association with subduction environments, should be considered in future studies on the petrogenesis of ultramafic bodies found in polymetamorphic Archaean terranes.

**Author Contributions:** T.M., K.S., G.P., I.N. and K.-I.T. conducted field surveys in southern West Greenland. I.N., Y.H., J.M.G. and A.T. analyzed chemical compositions of minerals. T.M. prepared the manuscript.

**Funding:** This study was financially supported by a Grant-in-Aid for Scientific Research of the Ministry of Education Culture, Sports, Science and Technology of Japan (No. 16H05741: TM), Kanazawa University SAKIGAKE 2018 (T.M.) and by the Carlsberg Foundation (K.S.)

**Acknowledgments:** We are grateful to S. Umino and T. Mizukami for discussions. Review comments from anonymous reviewers and a journal editor significantly improved the revised version of the manuscript.

**Conflicts of Interest:** The authors declare no conflict of interest. The founding sponsors had no role in the design of the study; in the collection, analyses, or interpretation of data; in the writing of the manuscript, and in the decision to publish the results.

## References

1. Mcgregor, V.R.; Nutman, A.P.; Mcgregor, V.R.; Polytechnic, O. The late Archaean mobile belt through Godthåbsfjord, southern West Greenland: A continent-continent collision zone? *Bull. Geol. Soc. Denmark* **1991**, *39*, 179–197.
2. Road, S.; Friend, C.R.L.; Nutman, A.P. New pieces to the Archaean terrane jigsaw puzzle in the Nuuk region, southern West Greenland: Steps in transforming a simple insight into a complex regional tectonothermal model. *J. Geol. Soc. Lond.* **2005**, *162*, 147–162.
3. Chadwick, B.; Crewe, M.A. Chromite in the early Archean Akilia association (ca. 3,800 MY), Ivisartoq region, inner Godthåbsfjord, southern West Greenland. *Econ. Geol.* **1986**, *81*, 184–191. [[CrossRef](#)]
4. Dymek, R.F.; Brothers, S.C.; Craig, M. Petrogenesis of Ultramafic Metamorphic Rocks from. *J. Petrol.* **1988**, *29*, 1353–1397. [[CrossRef](#)]
5. Garde, A.A.; Garde, A.A. *Accretion and Evolution of an Archaean High-Grade Grey Gneiss—Amphibolite Complex: The Fiskefjord Area, Southern West Greenland*; Geological Survey of Denmark and Greenland, Ministry of Environment and Energy: Copenhagen, Denmark, 1997; Volume 177, ISBN 8778710197.
6. Friend, C.; Bennett, V.; Nutman, A. Abyssal peridotites >3,800 Ma from southern West Greenland: Field relationships, petrography, geochronology, whole-rock and mineral chemistry of dunite and harzburgite inclusions in the Itsaq Gneiss Complex. *Contrib. Mineral. Petrol.* **2002**, *143*, 71–92. [[CrossRef](#)]
7. Nutman, A.P.; Friend, C.R.L. New 1:20,000 scale geological maps, synthesis and history of investigation of the Isua supracrustal belt and adjacent orthogneisses, southern West Greenland: A glimpse of Eoarchean crust formation and orogeny. *Precambrian Res.* **2009**, *172*, 189–211. [[CrossRef](#)]
8. Szilas, K.; Kelemen, P.B.; Rosing, M.T. The petrogenesis of ultramafic rocks in the >3.7Ga Isua supracrustal belt, southern West Greenland: Geochemical evidence for two distinct magmatic cumulate trends. *Gondwana Res.* **2015**, *28*, 565–580. [[CrossRef](#)]
9. Szilas, K.; Van Hinsberg, V.; McDonald, I.; Næraa, T.; Rollinson, H.; Adetunji, J.; Bird, D. Geoscience Frontiers Highly refractory Archaean peridotite cumulates: Petrology and geochemistry of the Seqi Ultramafic Complex, SW Greenland. *Geosci. Front.* **2018**, *9*, 689–714. [[CrossRef](#)]
10. van de Löcht, J.; Hoffmann, J.E.; Li, C.; Wang, Z.; Becker, H.; Rosing, M.T.; Kleinschrodt, R.; Münker, C. Earth's oldest mantle peridotites show entire record of late accretion. *Geology* **2018**, *46*, 199–202. [[CrossRef](#)]
11. Szilas, K.; Van Hinsberg, V.J.; Creaser, R.A.; Kisters, A.F.M. The geochemical composition of serpentinites in the Mesoarchaeon Tartoq Group, SW Greenland: Harzburgitic cumulates or melt-modified mantle? *Lithos* **2014**, *198–199*, 103–116. [[CrossRef](#)]
12. Friend, C.R.L.; Nutman, A.P. Dunites from Isua, Greenland: A ca. 3720 Ma window into subcrustal metasomatism of depleted mantle. *Geology* **2011**, *39*, 663–666. [[CrossRef](#)]
13. Rollinson, H. Recognising early Archaean mantle: A reappraisal. *Contrib. Mineral. Petrol.* **2007**, *154*, 241–252. [[CrossRef](#)]
14. Pons, M.-L.; Quitte, G.; Fujii, T.; Rosing, M.T.; Reynard, B.; Moynier, F.; Douchet, C.; Albarede, F. Early Archean serpentine mud volcanoes at Isua, Greenland, as a niche for early life. *Proc. Natl. Acad. Sci. USA* **2011**, *108*, 17639–17643. [[CrossRef](#)]
15. Szilas, K.; Kelemen, P.B.; Bernstein, S. Peridotite enclaves hosted by Mesoarchaeon TTG-suite orthogneisses in the Fiskefjord region of southern West Greenland. *GeoResJ* **2015**, *7*, 22–34. [[CrossRef](#)]
16. Kaczmarek, M.; Reddy, S.M.; Nutman, A.P.; Friend, C.R.L.; Bennett, V.C. Earth's oldest mantle fabrics indicate Eoarchaeon subduction. *Nat. Commun.* **2016**, *7*, 1–7. [[CrossRef](#)]
17. Rosing, M.T. Metasomatic alteration of ultramafic rocks. In *Fluid Movements—Element Transport and the Composition of the Deep Crust*; Kluwer Academic Publishers: Dordrecht, The Netherlands, 1989; pp. 187–202.
18. Rose, N.M.; Rosing, M.T.; Bridgwater, D. The origin of metacarbonate rocks in the Archaean Isua supracrustal belt, West Greenland. *Am. J. Sci.* **1996**, *296*, 1004–1044. [[CrossRef](#)]
19. Ribbe, P.H. Titanium, fluorine, and hydroxyl in the humite minerals. *Am. Mineral.* **1979**, *64*, 1027–1035.
20. Fujino, K.; Takeuchi, Y. Crystal chemistry of titanian chondrodite and titanian clinohumite of high-pressure origin. *Am. Mineral.* **1978**, *63*, 535–543.
21. Jones, N.W. Crystallographic nomenclature and twinning in the humite minerals. *Am. Mineral.* **1969**, *54*, 309–313.

22. Aoki, K.; Fujino, K.; Akaogi, M. Mineralogy and Petrology Titanohondrodite and Titanoeilinohumite Derived from the Upper Mantle in the Buell Park Kimberlite, Arizona, USA. *Contrib. Mineral. Petrol.* **1976**, *253*, 243–253. [[CrossRef](#)]
23. Mcgetchin, T.R.; Silver, L.T.; Chodos, A.A. Titanoclinohumite' A possible Mineralogical site for water in the Upper Mantle. *J. Geophys. Res.* **1970**, *75*, 255–259. [[CrossRef](#)]
24. Dymek, R.F.; Boak, J.L.; Brothers, S.C. Titanian chondrodite- and titanian clinohumite-bearing metadunite from the 3800 Ma Isua supracrustal belt West Greenland: Chemistry, petrology, and origin. *Am. Mineral.* **1988**, *73*, 547–558.
25. Smith, D. Chlorite-rich ultramafic reaction zones in Colorado Plateau xenoliths: Recorders of sub-Moho hydration. *Contrib. Mineral. Petrol.* **1995**, *121*, 185–200. [[CrossRef](#)]
26. Kogarko, L.N.; Kurat, G.; Ntaflos, T. Henrymeyerite in the metasomatized upper mantle of eastern Antarctica. *Can. Mineral.* **2007**, *45*, 497–501. [[CrossRef](#)]
27. Möckel, J.R. Structural petrology of the garnet-peridotite of Alpe Arami (Ticino, Switzerland). *Leidse Geol. Meded.* **1969**, *42*, 61–130.
28. Ishibashi, K.; Miyahisa, M.; Sasaki, M. Titanoclinohumite from Fujiwara complex in the Higashi-akaishi Mountainland, Shikoku, Japan. *J. Mineral. Petrol. Econ. Geol.* **1978**, *78*, 18–25. [[CrossRef](#)]
29. Trommsdorff, V.; Evans, B.W. Titanian hydroxyl-clinohumite: Formation and breakdown in antigorite rocks (Malenco, Italy). *Contrib. Mineral. Petrol.* **1980**, *72*, 229–242. [[CrossRef](#)]
30. Scamburli, M.; Hoogerduijn Strating, E.H.; Piccardo, G.B.; Vissers, R.L.M.; Rampone, E. Alpine olivine- and titanian clinohumite-bearing assemblages in the Erro-Tobbio peridotite (Voltri Massif, NW Italy). *J. Metamorph. Geol.* **1991**, *9*, 79–91.
31. Shen, T.; Hermann, J.; Zhang, L.; Lü, Z.; Padrón-Navarta, J.A.; Xia, B.; Bader, T. UHP Metamorphism Documented in Ti-chondrodite- and Ti-clinohumite-bearing Serpentinized Ultramafic Rocks from Chinese Southwestern Tianshan. *J. Petrol.* **2015**, *56*, 1425–1458. [[CrossRef](#)]
32. Zhang, R.Y.; Liou, J.G.; Cong, B.L. Talc-, magnesite- and ti-clinohumite-bearing ultrahigh-pressure meta-mafic and ultramafic complex in the dabie mountains, China. *J. Petrol.* **1995**, *36*, 1011–1037. [[CrossRef](#)]
33. Rahn, M.K.; Bucher, K. Petrology Titanian clinohumite formation in the Zermatt-Sl as ophiolites, Central Alps. *Mineral. Petrol.* **1998**, *64*, 1–13. [[CrossRef](#)]
34. Zhang, R.Y.; Li, T.; Rumble, D.; Yui, T.F.; Li, L.; Yang, J.S.; Pan, Y.; Liou, J.G. Multiple metasomatism in Sulu ultrahigh-P garnet peridotite constrained by petrological and geochemical investigations. *J. Metamorph. Geol.* **2007**, *25*, 149–164. [[CrossRef](#)]
35. Evans, B.W.; Trommsdorff, V. Fluorine hydroxyl titanian clinohumite in Alpine recrystallized garnet peridotite: Compositional controls and petrologic significance. *Am. J. Sci.* **1983**, *283A*, 355–369.
36. López Sánchez-Vizcaíno, V.; Trommsdorff, V.; Gómez-Pugnaire, M.T.; Garrido, C.J.; Müntener, O.; Connolly, J.A.D. Petrology of titanian clinohumite and olivine at the high-pressure breakdown of antigorite serpentinite to chlorite harzburgite (Almirez Massif, S. Spain). *Contrib. Mineral. Petrol.* **2005**, *149*, 627–646. [[CrossRef](#)]
37. Garde, A.A.; Friend, C.R.L.; Nutman, A.P.; Marker, M. Rapid maturation and stabilisation of middle Archaean continental crust: Rapid maturation and stabilisation of middle Archaean continental crust: The Akia terrane, southern West Greenland. *Bull. Geol. Soc. Denmark* **2000**, *47*, 1–27.
38. Kirkland, C.L.; Yakymchuk, C.; Hollis, J.; Heide-Jørgensen, H.; Danišić, M. Mesoarchean exhumation of the Akia terrane and a common Neoproterozoic tectonothermal history for West Greenland. *Precambrian Res.* **2018**, *314*, 129–144. [[CrossRef](#)]
39. Gardiner, N.J.; Kirkland, C.L.; Hollis, J.; Szilas, K.; Steenfelt, A.; Yakymchuk, C.; Heide-Jørgensen, H. Building Mesoarchean crust upon Eoarchean roots: The Akia Terrane, West Greenland. *Contrib. Mineral. Petrol.* **2019**, *174*, 20. [[CrossRef](#)]
40. Guotana, J.M.; Morishita, T.; Yamaguchi, R.; Nishio, I.; Tamura, A.; Tani, K.; Harigane, Y.; Szilas, K.; Pearson, D.; Yamaguchi, R. Contrasting textural and chemical signatures of chromitites in the Mesoarchean Ulamertoq peridotite body, southern West Greenland. *Geosciences* **2018**, *8*, 328. [[CrossRef](#)]
41. Morishita, T.; Arai, S.; Tamura, A. Petrology of an apatite-rich layer in the Finero phlogopite—Peridotite, Italian Western Alps; implications for evolution of a metasomatising agent. *Lithos* **2003**, *69*, 37–49. [[CrossRef](#)]

42. Morishita, T.; Tani, K.-I.I.; Soda, Y.; Tamura, A.; Mizukami, T.; Ghosh, B. The uppermost mantle section below a remnant proto-Philippine Sea island arc: Insights from the peridotite fragments from the Daito Ridge. *Am. Mineral.* **2018**, *103*, 1151–1160. [[CrossRef](#)]
43. Pearce, N.J.G.; Perkins, W.T.; Westgate, J.A.; Gorton, M.P.; Jackson, S.E.; Neal, C.R.; Chenery, S.P. A Compilation of New and Published Major and Trace Element Data for NIST SRM 610 and NIST SRM 612 Glass Reference Materials. *Geostand. Geoanalytical Res.* **1997**, *21*, 115–144. [[CrossRef](#)]
44. Longerich, H.P.; Gu, D.; Jackson, S.E.; Gü, D. Elemental fractionation in laser ablation inductively coupled plasma mass spectrometry. *Fresenius J. Anal. Chem.* **1996**, *355*, 538–542. [[CrossRef](#)] [[PubMed](#)]
45. Morishita, T.; Ishida, Y.; Arai, S.; Shirasaka, M. Determination of multiple trace element compositions in thin (<30  $\mu\text{m}$ ) layers of NIST SRM 614 and 616 using laser ablation-inductively coupled plasma-mass spectrometry (LA-ICP-MS). *Geostand. Geoanal. Res.* **2005**, *29*, 107–122. [[CrossRef](#)]
46. Warren, J.M. Global variations in abyssal peridotite compositions. *Lithos* **2016**, *248–251*, 193–219. [[CrossRef](#)]
47. Wunder, B. Equilibrium experiments in the system  $\text{MgO} \pm \text{SiO}_2 \pm \text{H}_2\text{O}$  (MSH): Stability fields of clinohumite-OH [ $\text{Mg}_9\text{Si}_4\text{O}_{16}(\text{OH})_2$ ], chondrodite-OH [ $\text{Mg}_5\text{Si}_2\text{O}_8(\text{OH})_2$ ] and phase A ( $\text{Mg}_7\text{Si}_2\text{O}_8(\text{OH})_6$ ). *Contrib. Mineral. Petrol.* **1998**, *132*, 111–120. [[CrossRef](#)]
48. Luoni, P.; Rebay, G.; Spalla, M.I.; Zannoni, D. UHP Ti-chondrodite in the Zermatt-Saas serpentinite: Constraints on a new tectonic scenario. *Am. Mineral.* **2018**, *103*, 1002–1005. [[CrossRef](#)]
49. Engi, M.; Lindsley, D.H. Stability of titanian clinohumite: Experiments and thermodynamic analysis. *Contrib. Mineral. Petrol.* **1980**, *72*, 415–424. [[CrossRef](#)]
50. Fumagalli, P.; Poli, S.; Fischer, J.; Merlini, M.; Gemmi, M. The high-pressure stability of chlorite and other hydrates in subduction mélanges: Experiments in the system  $\text{Cr}_2\text{O}_3\text{-MgO-Al}_2\text{O}_3\text{-SiO}_2\text{-H}_2\text{O}$ . *Contrib. Mineral. Petrol.* **2014**, *167*, 1–16. [[CrossRef](#)]
51. Weiss, M. Clinohumites: A Field and Experimental Study. Ph.D. Thesis, Swiss Federal Institute of Technology, Zurich, Switzerland, 1997. No. 12202.
52. Brey, G.; Brice, W.R.; Ellis, D.J.; Green, D.H.; Harris, K.L.; Ryabchikov, I.D. Pyroxene-carbonate reactions in the upper mantle. *Earth Planet. Sci. Lett.* **1983**, *62*, 63–74. [[CrossRef](#)]
53. Bucher, K.; Frey, M. *Petrogenesis of Metamorphic Rocks*; Springer: Berlin/Heidelberg, Germany, 2002; ISBN 978-3-662-04916-7.
54. Trommsdorff, V.; Evans, B.W. Antigorite-ophicarbonates: Phase relations in a portion of the system  $\text{CaO-MgO-SiO}_2\text{-H}_2\text{O-CO}_2$ . *Contrib. Mineral. Petrol.* **1977**, *60*, 39–56. [[CrossRef](#)]
55. Ulmer, P.; Trommsdorff, V. Phase relations of hydrous mantle subducting to 300 km. *Spec. Publ. Geochem. Soc.* **1999**, *6*, 259–282.
56. Scott, J.M.; Liu, J.; Pearson, D.G.; Waight, T.E. Mantle depletion and metasomatism recorded in orthopyroxene in highly depleted peridotites. *Chem. Geol.* **2016**, *441*, 280–291. [[CrossRef](#)]
57. Frost, R. Contact Metamorphism of Serpentine, Chloritic Blackwall and Rodingite at Paddy-Go-Easy Pass, Central Cascades, Washington. *J. Petrol.* **1975**, *16*, 272–313. [[CrossRef](#)]
58. Trommsdorff, V.; Sánchez-Vizcaíno, V.L.; Gomez-Pugnaire, M.T.; Müntener, O. High pressure breakdown of antigorite to spinifex-textured olivine and orthopyroxene, SE Spain. *Contrib. Mineral. Petrol.* **1998**, *132*, 139–148. [[CrossRef](#)]
59. Arai, S. “Non-calciferous” orthopyroxene and its bearing on the petrogenesis of ultramafic rocks in Sangun and Joetsu zones. *J. Jpn. Assoc. Mineral. Petrol. Econ. Geol.* **1974**, *69*, 343–353. [[CrossRef](#)]
60. Arai, S. Contact metamorphosed dunite-harzburgite complex in the Chugoku district, western Japan. *Contrib. Mineral. Petrol.* **1975**, *52*, 1–16. [[CrossRef](#)]
61. Zhang, R.Y.; Shu, J.F.; Mao, H.K.; Liou, J.G. Magnetite lamellae in olivine and clinohumite from Dabie UHP ultramafic rocks, central China. *Am. Mineral.* **1999**, *84*, 564–569. [[CrossRef](#)]
62. Connolly, J.A.D. Computation of phase equilibria by linear programming: A tool for geodynamic modeling and its application to subduction zone decarbonation. *Earth Planet. Sci. Lett.* **2005**, *236*, 524–541. [[CrossRef](#)]
63. Arai, S.; Ishimaru, S.; Okrugin, V.M. Metasomatized harzburgite xenoliths from Avacha volcano as fragments of mantle wedge of the Kamchatka arc: Implication for the metasomatic agent. *Isl. Arc* **2003**, *12*, 233–246. [[CrossRef](#)]
64. Arai, S.; Kida, M. Origin of fine-grained peridotite xenoliths from Iraya volcano of Batan Island, Philippines: Deserpentinization or metasomatism at the wedge mantle beneath an incipient arc? *Isl. Arc* **2008**, *9*, 458–471. [[CrossRef](#)]

65. McInnes, B.I.; Gregoire, M.; Binns, R.A.; Herzig, P.M.; Hannington, M.D. Hydrous metasomatism of oceanic sub-arc mantle, Lihir, Papua New Guinea: Petrology and geochemistry of fluid-metasomatised mantle wedge xenoliths. *Earth Planet. Sci. Lett.* **2001**, *188*, 169–183. [[CrossRef](#)]
66. Iizuka, Y.; Nakamura, E. Experimental Study for of the Slab-mantle Interaction and Implications the Formation of Titanoclinohumite at Deep Subduction Zone subducting oceanic crust ( denoted as slab ) and the overlying wedge mantle in the subduction zone, respectively. *The chemi. Proc. Jpn. Acad.* **1995**, 159–164. [[CrossRef](#)]
67. Vance, J.A.; Dungan, M.A. Formation of peridotites by deserpentinization in the Darrington and Sultan areas, Cascade Mountains, Washington. *Geol. Soc. Am. Bull.* **1977**, *88*, 1497. [[CrossRef](#)]
68. Yang, J. Deep subduction of mantle-derived garnet peridotites from the Su-Lu UHP metamorphic terrane in China. *J. Metamorph. Geol.* **2000**, *18*, 167–180. [[CrossRef](#)]
69. Polat, A.; Wang, L.; Appel, P.W.U. A review of structural patterns and melting processes in the Archean craton of West Greenland: Evidence for crustal growth at convergent plate margins as opposed to non-uniformitarian models. *Tectonophysics* **2015**, *662*, 67–94. [[CrossRef](#)]



© 2019 by the authors. Licensee MDPI, Basel, Switzerland. This article is an open access article distributed under the terms and conditions of the Creative Commons Attribution (CC BY) license (<http://creativecommons.org/licenses/by/4.0/>).